

GMMMap: Memory-Efficient Continuous Occupancy Map Using Gaussian Mixture Model

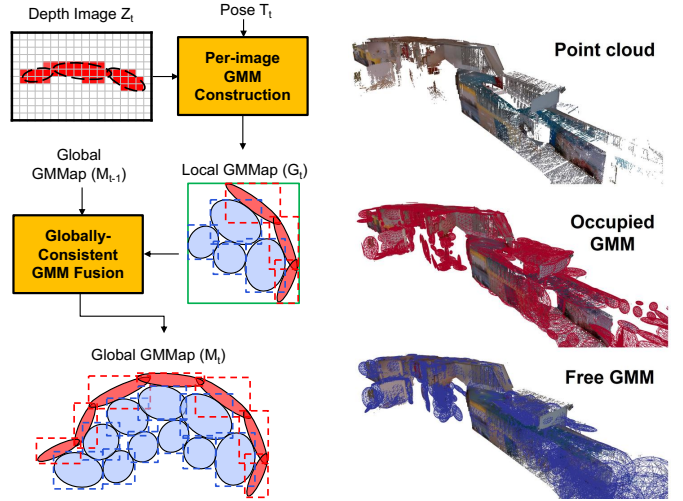
Peter Zhi Xuan Li¹, Sertac Karaman¹, *Member, IEEE Student Member, IEEE*, Vivienne Sze¹, *Senior Member, IEEE*,

Abstract—Energy consumption of memory accesses dominates the compute energy in energy-constrained robots which require a compact 3D map of the environment to achieve autonomy. Recent mapping frameworks only focused on reducing the map size while incurring significant memory usage during map construction due to multi-pass processing of each depth image. In this work, we present a memory-efficient continuous occupancy map, named GMMMap, that accurately models the 3D environment using a Gaussian Mixture Model (GMM). Memory-efficient GMMMap construction is enabled by the single-pass compression of depth images into local GMMs which are directly fused together into a globally-consistent map. By extending Gaussian Mixture Regression to model unexplored regions, occupancy probability is directly computed from Gaussians. Using a low-power ARM Cortex A57 CPU, GMMMap can be constructed in real-time at up to 60 images per second. Compared with prior works, GMMMap maintains high accuracy while reducing the map size by at least 56%, memory overhead by at least 88%, DRAM access by at least 78%, and energy consumption by at least 69%. Thus, GMMMap enables real-time 3D mapping on energy-constrained robots.

Index Terms—Mapping, RGB-D Perception, Sensor Fusion, Memory Efficiency

I. INTRODUCTION

ENERGY-constrained microrobots [1]–[3] could enable a wide variety of applications, from autonomous navigation, search and rescue, and space exploration. Due to the limited battery capacity onboard these robots, the amount of energy available for computation is extremely limited and could be dominated by memory accesses. For instance, the energy required for accessing on-chip memory (*e.g.*, cache) is more than an order-of-magnitude higher than that when performing a 32-bit multiplication [4]. The energy consumption of memory access increases with the size and distance of the memory from the processor. Within the same chip, accessing a higher-level L2 cache (a few MBs) requires up to an order-of-magnitude more energy than lower-level L0 and L1 caches (a few KBs). However, accessing data stored in a larger, off-chip memory such as DRAM (GBs of storage) requires more than two orders-of-magnitude higher energy than smaller, on-chip (local) CPU caches [4]. The memory (capacity) usage of an algorithm is not only consisted of output variables but also input and temporary variables allocated during computation. Thus, algorithms designed for many robotics applications, especially the ones involving energy-constrained



(a) Incremental construction of the GMMMap from a depth image Z_t and pose T_t obtained at time t . Each depth image is compressed into a local GMMMap G_t which is then fused with current global GMMMap M_{t-1} . (b) Visualization of the first floor of the MIT Stata Center and its GMMMap representation consisting of GMMs representing occupied (red) and free (blue) regions. Each Gaussian is visualized as an ellipsoid in 3D.

Fig. 1. Illustration of GMMMap’s (a) memory-efficient construction procedure and (b) representation for the MIT’s Stata Center. GMMs representing occupied and free regions in the environment are illustrated by red and blue ellipsoids, respectively. The GMMMap models a continuous distribution of occupancy in the State Center while requiring only 296KB to store.

robots, should be *memory efficient* during computation such that: *i*) the number of *memory accesses* do not dominate the algorithm; *ii*) amount of *memory (capacity) overhead* for storing input and temporary variables will be small enough to remain in energy-efficient lower-level caches.

For mapping algorithms, both memory overhead and accesses could easily dominate. During map construction, the multi-pass processing of sensor measurements requires them to be stored (*i.e.*, as input and temporary variables) entirely in memory to support repeated accesses, which increases overhead and reduces the remaining memory for map storage. Incrementally updating/reconstructing a previously-observed region in the map is typically performed by casting rays associated with all sensor measurements into the map. Since these rays diverge away from the sensor origin, memory accesses along these rays often lack the (spatial and temporal) locality required for effective cache usage, and thus require a significant number of memory accesses to DRAM. Thus, achieving memory efficiency is both crucial and challenging for mapping algorithms.

Authors are with the Massachusetts Institute of Technology, Cambridge, MA 02139, USA. Emails: {peterli, sertac, sze}@mit.edu. This work was partially funded by the NSF RTML 1937501 and the NSF CPS 1837212.

In addition to achieving memory efficiency, the resulting map should satisfy the following requirements to enable memory-efficient, real-time processing of a variety of downstream applications that enable autonomy.

- 1) **Compactness:** A compact map can represent a larger portion of the environment in both on-chip (cache) and off-chip memory (DRAM). When accessing a region of the environment that does not reside in the cache, a compact map also reduces the number of energy-intensive DRAM accesses required to update the cache.
- 2) **Modeling unexplored regions:** In autonomous exploration, the robot seeks to minimize the number of unexplored regions while traversing in obstacle-free regions. Thus, the ability to determine and update the regions that are currently unexplored enables state-of-the-art autonomous exploration algorithms based on frontier [5] or mutual information [6], [7].
- 3) **Query compute efficiency:** During path planning and autonomous exploration, the robot needs to query multiple locations in the map to determine the current state of the environment [8]. The results of these queries are often used to make decisions, such as the next location to travel, in real time. Thus, the state of the environment should be efficiently computed from the map.

Current state-of-the-art mapping frameworks require the probabilistic modeling of *occupancy* (*i.e.*, whether or not an obstacle exists) at every location in the 3D environment. These frameworks can be classified based on their underlying probabilistic models used to infer occupancy. For instance, the well-known framework, OctoMap [9], contains a set of Bernoulli random variables for modeling the occupancy at a discrete set of homogeneous regions in the environment. Even though OctoMap could model unexplored space and achieve query efficiency, OctoMap is not compact enough for storage on energy-constrained robots. By using more compact models (*e.g.*, set of Gaussians or kernels), recent frameworks (*e.g.*, NDT-OM [10], Hilbert Map [11], HGMM [12]) only focused on reducing the map size while incurring significant memory overhead and accesses for multi-pass processing of raw sensor measurements in nearly every stage of the mapping pipeline. In addition, the resulting maps produced by these frameworks cannot satisfy all of the above-mentioned requirements for enabling efficient downstream applications.

In this paper, we propose a continuous occupancy map comprised of a compact Gaussian Mixture Model (GMM), named GMMMap, that is efficiently and accurately constructed from a sequence of depth images and poses of a robot. To achieve significantly higher memory efficiency than prior works, our GMMMap accurately compresses each depth image into a compact GMM in a *single pass*, and *directly* operates on Gaussians in the GMM (*i.e.*, without other intermediate representations) for all remaining mapping operations. Our contributions are summarized as follows:

- 1) **Single-pass compression:** A *single-pass* procedure that accurately compresses a depth image into a local GMM representing both free and occupied regions. Prior works [11]–[16] require significant overhead for

storing the entire image in memory due to *multi-pass* processing.

- 2) **Gaussian-direct map construction:** A novel procedure that *directly* fuses the local GMMs across multiple images into a globally-consistent GMM without casting sensor rays (*i.e.*, one ray for each pixel in the depth image) into the map. Prior works [9], [10], [12], [17] requires a significant number of memory accesses during ray casting in order to update the previously-observed region that intersects with all sensor rays.
- 3) **Gaussian-direct occupancy query:** An extension of Gaussian Mixture Regression to *directly* compute occupancy from GMM while accounting for unexplored regions. Prior works require constructing and storing intermediate representations for modeling unexplored regions [11], [14] or do not model them at all [12].

In our previous work [18], we proposed the Single-Pass Gaussian Fitting (SPGF) algorithm that enables single-pass compression of depth image into a GMM representing only the occupied region (*i.e.*, a part of the first contribution) but not the obstacle-free region. In this work, we not only extend our previous work to also construct a GMM representing the free region (*i.e.*, the first contribution) but also illustrate how to directly operate on Gaussians during map construction and occupancy query (*i.e.*, the second and third contribution). An overview of the GMMMap and its representation for the first floor of MIT’s Stata Center are illustrated in Fig. 1.

This paper is organized as follows. After analyzing existing works in Section II, we describe how the occupancy is compactly represented and efficiently estimated from our GMMMap in Section III. Memory-efficient algorithms that incrementally and accurately construct the GMMMap given a sequence of depth images are presented in Section IV. Finally, we validate GMMMap against existing works in terms of mapping accuracy, memory footprint, throughput and energy consumption across multiple environments in Section V.

II. RELATED WORKS

Constructing an accurate and compact representation of the 3D environment is crucial for enabling many downstream robotics applications such as path planning and autonomous exploration. During the past few decades, many frameworks proposed different models to represent the distribution of the occupancy probability (*i.e.*, the likelihood that a region contains an obstacle) across the 3D environment. These models exhibit different trade-offs in memory and computational efficiency during the construction and querying of the map.

Discrete representations: Some of the most popular mapping frameworks discretize the environment into cubic regions (*i.e.*, grids in 2D and voxels in 3D) such that each region contains a Bernoulli random variable representing the occupancy probability and is assumed to be spatially independent of each other. One of the earliest 2D mapping frameworks, the occupancy grid map [19], discretizes the environments into equally-sized grids. However, the map size is prohibitively large in 3D because the size scales cubically with the dimensions of the voxels and the environment. To reduce map

size in 3D, OctoMap [9] stores the occupancy probabilities in voxels whose sizes can adapt to homogeneous regions in the environment. Like other similar discrete representations such as [19], [20], OctoMap suffers from artifacts associated with voxelization and requires a significant amount of memory accesses during construction. To incrementally construct the map given a set of sensor rays (more than 300,000 in each 640×480 depth image), each ray is cast into the map to update the subset of voxels such rays intersect. Since these rays diverge away from the sensor origin, memory accesses along these rays often lack spatial and temporal locality (especially if the map is too large to fit within on-chip caches). Since OctoMap is often not compact, updating the map requires a significant amount of memory accesses (more than 300,000 per image) to off-chip DRAM.

Non-parametric representations: To relax the spatial independence assumption in discrete map representations, Gaussian process (GP) was proposed to estimate a continuous distribution of occupancy [21] using a covariance function that captures the spatial correlation among all sensor measurements. Since GP requires the storage of *all* sensor measurements (since the beginning of the robotics experiment) to update the covariance function, the memory overhead scales with the total number of measurements N . During a map query, the covariance function generates a large matrix that requires $O(N^3)$ to invert, which greatly reduces the query efficiency. To enable faster map construction and query, recent non-parametric methods such as GPOctoMap [22] and BGKOctoMap-L [17] discretize the environment into blocks of octrees (*i.e.*, a test-data octree). For subsets of measurements (*i.e.*, training data) that lie within each block, GPOctoMap and BGKOctoMap-L update the octrees in each block and its neighbors (*i.e.*, extended blocks) using GP and Bayesian Generalized Kernel (BGK) inference, respectively. Similar to OctoMap, both GPOctoMap and BGKOctoMap-L directly operate on sensor rays that are cast into the map during incremental construction and require significant memory accesses to DRAM. In addition, both frameworks require the storage of training data for each block during map construction which incurs significantly larger memory overhead than OctoMap.

Semi-parametric representations: To create an extremely compact representation of the environment, several frameworks compress the sensor measurements using a set of parametric functions (*e.g.*, Gaussians or other kernels) which are then used to infer occupancy. One of the well-known semi-parametric representations is the Normal Distribution Transform Occupancy Map (NDT-OM) [10] that partitions the environment into large voxels such that measurements within each voxel are represented by a Gaussian. Since measurements within a voxel could belong to multiple objects, representing them with a single Gaussian often leads to a loss of accuracy in the resulting map. Similar to OctoMap, NDT-OM requires significant memory access to DRAM due to the casting of sensor rays into the map during construction.

To further reduce map size, recent frameworks, such as Hilbert Map (HM) [11], Variable Resolution GMM (VRGMM) map [14], Hierarchical GMM (HGMM) map [12], compress sensor rays into special kernels (in HM) or Gaussians (in

VRGMM and HGMM). Such compression is performed using techniques such as Quick-Means (QM) [11], Hierarchical Expectation-Maximization (H-EM) [13], Region Growing (RG) [15], and Self-Organizing GMMs (SOGMM) [16]. However, these techniques require significant memory overhead to store all sensor measurements (more than 300,000 pixels in a 640×480 depth image) due to their *multi-pass* processing. Even though the resulting maps are compact after compression, they either could not model unexplored regions (in HGMM), or require online training (for a logistic regression classifier in HM) and intermediate representations to model these regions (using Monte Carlo sampling to create an intermediate grid map in VRGMM). Even though our GMMap is also classified as a semi-parametric representation, we can accurately construct and query the map directly using Gaussians (while preserving unexplored regions) to reduce memory overhead and accesses.

III. OCCUPANCY REPRESENTATION & ESTIMATION

In this section, we describe how to compactly model a continuous distribution of occupancy using a Gaussian Mixture Model (GMM) in the proposed GMMap. In addition, we illustrate how to directly estimate the occupancy probability from Gaussians using Gaussian Mixture Regression (GMR) while accounting for the initial unknown state of the environment so that the unexplored regions are preserved.

Let $X \in \mathbb{R}^3$ denote the 3D coordinate in the world frame. Let $O \in \mathbb{R}$ denote the occupancy value such that regions with values greater than one are occupied with obstacles, and regions with values less than zero are obstacle free. In addition, unexplored regions have an occupancy value near 0.5. Let P denote the joint random variable such that

$$P = \begin{bmatrix} X \\ O \end{bmatrix}. \quad (1)$$

The map of the 3D environment is represented by the following GMM which is an *unnormalized* distribution for the joint variable P , *i.e.*,

$$M_P(p) \sim \sum_{i=1}^K \pi_i \mathcal{N}(p \mid \mu_i, \Sigma_i), \quad (2)$$

where K is the number of Gaussians. The weight π_i , mean μ_i , and covariance Σ_i are the parameters of the i th Gaussian such that

$$\mu_i = \begin{bmatrix} \mu_{iX} \\ \mu_{iO} \end{bmatrix}, \quad \Sigma_i = \begin{bmatrix} \Sigma_{iX} & \Sigma_{iXO} \\ \Sigma_{iOX} & \Sigma_{iO} \end{bmatrix}. \quad (3)$$

Note that the GMM in Eqn. (2) can be compactly stored because each Gaussian is parameterized by μ_i , Σ_i , and π_i . For the rest of the paper, we drop the index i for all variables when we refer to any Gaussian in the GMM.

During the experiment, the robot makes a sequence of range measurements. Each range measurement consists of a ray that originates from the robot, passes through a free region, and ends at the surface of an obstacle (occupied region). Regions that are traversed by all such rays are *observed* by the robot. We determine the parameters of the GMM in Eqn. (2) using range measurements such that it compactly models all

observed regions. Thus, regions that have not been observed (*i.e.*, unexplored) cannot be modeled by the GMM alone.

To compactly model the unexplored region, we use the *unexplored prior* $Q_{O|X}$ with its weight π_0 to represent the initial unknown state of the entire environment, *i.e.*,

$$Q_{O|X}(o | x) = \mathcal{N}(o | \mu_0, \sigma_0^2), \quad (4)$$

where

$$\mu_0 = 0.5, \quad \sigma_0^2 = 0.25. \quad (5)$$

The weight π_0 should be set to a large value such that measurements from multiple timesteps are required to shift the occupancy value of an unexplored region (*i.e.*, 0.5) towards zero (free region) or one (occupied region) during GMR.

Unlike prior semi-parametric representations that estimate occupancy probability using either a classifier that requires additional online training [11], [23] or intermediate representations that require additional memory overhead [14], we efficiently preserve these regions by incorporating the unexplored prior into the Gaussian Mixture Regression (GMR) [24]. We describe the GMR procedure used to estimate occupancy directly from Gaussians as follows.

Using the GMM in Eqn. (2) and the unexplored prior in Eqn. (4), the occupancy O conditioned on the query location $X = x$ is computed as

$$P_{O|X}(o | x) = \sum_{i=0}^K \omega_i(x) \mathcal{N}(o | m_i(x), \sigma_i^2(x)), \quad (6)$$

where

$$\omega_i(x) = \begin{cases} \frac{\pi_0}{\sum_{j=1}^K \pi_j \mathcal{N}(x | \mu_{jX}, \Sigma_{jX}) + \pi_0}, & \text{if } i = 0, \\ \frac{\pi_i \mathcal{N}(x | \mu_{iX}, \Sigma_{iX})}{\sum_{j=1}^K \pi_j \mathcal{N}(x | \mu_{jX}, \Sigma_{jX}) + \pi_0}, & \text{otherwise,} \end{cases} \quad (7)$$

$$m_i(x) = \begin{cases} \mu_0, & \text{if } i = 0, \\ \mu_{iO} + \Sigma_{iOX} \Sigma_{iX}^{-1} (x - \mu_{iX}), & \text{otherwise,} \end{cases} \quad (8)$$

$$\sigma_i^2(x) = \begin{cases} \sigma_0^2, & \text{if } i = 0, \\ \Sigma_{iO} - \Sigma_{iOX} \Sigma_{iX}^{-1} \Sigma_{iXO}, & \text{otherwise.} \end{cases} \quad (9)$$

The expected occupancy value and its variance at location x is regressed using GMR as

$$m(x) = \mathbb{E}[O|X = x] = \sum_{i=0}^K \omega_i(x) m_i(x), \quad (10)$$

$$v(x) = \text{Var}[O|X = x] = \sum_{i=0}^K \omega_i(x) (m_i(x) + \sigma_i^2(x)) - m(x)^2. \quad (11)$$

The occupancy value can transition suddenly across the boundaries separating occupied and free regions (*e.g.*, at surfaces of obstacles). To better capture such transitions, each Gaussian in the GMMap models either an occupied or free region, but not both. Thus, the set of Gaussians representing occupied regions is defined as *occupied Gaussians* with an occupancy value of *one* (*i.e.*, $\mu_O = 1$). In addition, the set of Gaussians representing free regions is defined as *free Gaussians* with an occupancy value of *zero* (*i.e.*, $\mu_O = 0$).

Representing occupied and free regions using separate sets of Gaussians also guarantees that the expectation $m(x)$ in Eqn. (10) is bounded within $[0, 1]$. Thus, the expectation $m(x)$ becomes the *occupancy probability* of the environment at the query location x . In addition, the covariance terms Σ_{XO} , Σ_{OX} and Σ_O in Eqn. (3) become zero for all Gaussians, which significantly simplifies the entire GMR procedure and reduces the memory required to store the Gaussians in our map.

Since each Gaussian distribution tapers off from its mean at an exponential rate, the entire GMR procedure from Eqn. (6) to (11) can be accurately and efficiently approximated using a small subset of Gaussians whose Mahalanobis distances between their means to the query location x are less than a threshold α_M , *i.e.*,

$$\sqrt{(x - \mu_X)^\top \Sigma_X^{-1} (x - \mu_X)} \leq \alpha_M, \quad (12)$$

where μ_X and Σ_X are parameters of a Gaussian defined in Eqn. (3). In our experiments, we chose $\alpha_M = 2$ to ensure that more than 95% of the Gaussian distribution is considered.

To efficiently obtain the subset of Gaussians that satisfies Eqn. (12) in $O(\log(K))$ time (where K is the total number of Gaussians), we store the GMMap using an R-tree [25] constructed with bounding boxes that are axis-aligned with the world frame. Since the surface that satisfies the equality in Eqn. (12) for each Gaussian can be visualized as an ellipsoid in 3D, the bounding box at the leaf node of the R-tree for each Gaussian is sized to enclose such ellipsoid. Across all figures, occupied and free Gaussians are represented by red and blue ellipsoids, respectively. The occupied and free Gaussians in GMMap with their corresponding bounding boxes (dotted rectangles) are illustrated at the bottom of Fig. 1a.

IV. MEMORY-EFFICIENT MAP CONSTRUCTION

In this section, we present a memory-efficient framework to construct the GMMap M (*i.e.*, Eqn. (2)). At each timestep t , we *incrementally* constructs the GMMap M by updating the previous GMMap M_{t-1} with current measurements from the depth image $Z_t \in \mathbb{R}^{U \times V}$ obtained at pose $T_t \in \text{SE}(3)$. As illustrated in Fig. 1a, our framework consists of the following two procedures executed sequentially for each depth image:

- 1) **Per-image GMM construction:** The depth image Z_t with width U and height V obtained at pose T_t is compressed into a compact local GMMap G_t . A memory-efficient algorithm is proposed in Section IV-B to perform such compression one pixel at a time in a *single pass* through the depth image. Memory overhead is greatly reduced by avoiding the storage of the entire depth image in memory which is required for prior multi-pass approaches [11]–[16].
- 2) **Globally-consistent GMM fusion:** The local GMMap G_t is fused into the previous global GMMap M_{t-1} to obtain the updated GMMap M_t . A memory-efficient algorithm is proposed in Section IV-C to perform such fusion *directly* using Gaussians. The amount of memory accesses is greatly reduced by avoiding casting rays (more than 300,000) from each 640×480 image into the map as seen in prior works [9], [10], [12], [17].

To efficiently update Gaussian parameters during the above-mentioned procedures with little memory overhead, we present preliminaries that illustrate *in-place* construction of Gaussians using the method of moments (MoM) [26] in Section IV-A.

A. Efficiently Updating Gaussian Parameters

In this section, we illustrate how to efficiently update the parameters of occupied and free Gaussians in-place given new measurements. In the method of moments (MoM) [26], the first and second moments of a Gaussian are intermediate representations of its mean and covariance, respectively. Let $P = [X, O]^\top$ denote the joint variable for the 3D coordinate X (with respect to the current sensor origin) and its occupancy O . The unnormalized first $m^{(1)}$ and second $m^{(2)}$ moments of each Gaussian are defined as

$$m^{(1)} = \xi \mathbb{E}[P], \quad m^{(2)} = \xi \mathbb{E}[P^2], \quad (13)$$

where ξ is a normalization constant. Thus, the mean μ and covariance Σ of each Gaussian defined in Eqn. (3) can be recovered *in-place* from the unnormalized moments as

$$\mu = \frac{1}{\xi} m^{(1)}, \quad \Sigma = \frac{1}{\xi} m^{(2)} - \mu \mu^\top. \quad (14)$$

Unnormalized moments can be incrementally updated without relying on past measurements (which do not need to be stored in memory). Thus, during map construction, the moments for each Gaussian are stored instead of its mean and covariance. Recall that from Section III, each measurement (ray) consists of a point (*i.e.*, end of a ray representing the surface of an obstacle) and a line (*i.e.*, from the sensor origin to the end of the ray representing free region). Fusing a *point* $p = [x, 1]^\top \in P$ into an occupied Gaussian is computed as

$$m^{(1)} \leftarrow m^{(1)} + p, \quad (15a)$$

$$m^{(2)} \leftarrow m^{(2)} + pp^\top, \quad (15b)$$

$$\xi \leftarrow \xi + 1. \quad (15c)$$

Fusing a *line* from the sensor origin to the endpoint $p = [x, 0]^\top$ into a free Gaussian is computed as

$$m^{(1)} \leftarrow m^{(1)} + \frac{\|p\|}{2} p, \quad (16a)$$

$$m^{(2)} \leftarrow m^{(2)} + \frac{\|p\|}{3} pp^\top, \quad (16b)$$

$$\xi \leftarrow \xi + \|p\|. \quad (16c)$$

Note that the second term on the right side of Eqn. (16a) and (16b) is the closed-form expression for the first and second moments of the line, respectively. Our closed-form expression is accurate and more computationally efficient than prior works [11], [12] that approximate both moments by using points sampled at a fixed interval along the line.

When regressing occupancy using GMR, the unnormalized weight π of each occupied or free Gaussian should represent the amount of occupied or free evidence in the region where such Gaussian resides. For each free Gaussian, its weight π equals to the total length of all line segments used during

construction. When a line from sensor origin to $p = [x, 0]^\top$ is fused into a free Gaussian, its weight π is updated as

$$\pi \leftarrow \pi + \|p\|. \quad (17)$$

To ensure that the occupancy regressed using GMR is meaningful, the weights for occupied Gaussians should have the same unit as those for the free Gaussians. Thus, when a new endpoint p is fused into an occupied Gaussian, its weight is also updated using Eqn. (17).

Lastly, the Gaussian containing the fusion of two occupied or free Gaussians indexed by i and j is computed as

$$m^{(1)} \leftarrow m_i^{(1)} + m_j^{(1)}, \quad (18a)$$

$$m^{(2)} \leftarrow m_i^{(2)} + m_j^{(2)}, \quad (18b)$$

$$\xi \leftarrow \xi_i + \xi_j, \quad (18c)$$

$$\pi \leftarrow \pi_i + \pi_j. \quad (18d)$$

B. Per-Image GMM Construction

As illustrated in Fig. 2, we present a single-pass algorithm that constructs a local GMM G_t given the depth image Z_t obtained at pose T_t . From Section III, occupied and free regions in the environment are separately modeled using occupied (visualized using red ellipsoids) and free (visualized using blue ellipsoids) Gaussians, respectively. Thus, our algorithm, described in Alg. 1, creates both types of Gaussians in the local map G_t by executing the following procedures sequentially:

- 1) **SPGF*** (Line 2 in Alg. 1) : A memory-efficient algorithm that constructs the occupied GMM $G_{t, \text{occ}}$ and a compact free GMM basis $F_{t, \text{free}}$ in a *single pass* through the image Z_t using only the endpoints of the sensor rays. As illustrated in Fig. 3, operations within SPGF* are extended from our prior work SPGF [18].
- 2) **Construct Free GMM** (Line 3 in Alg. 1): By only considering the endpoints of the sensor rays in SPGF*, Gaussians represented by the free GMM basis $F_{t, \text{free}}$ cannot represent free region encoded within the camera frustum very well (see Fig. 4a). Thus, the basis $F_{t, \text{free}}$ is processed to construct the free GMM $G_{t, \text{free}}$ that better represents the free region (see Fig. 4b).
- 3) **Construct Local Map** (Lines 4 to 6 in Alg. 1): Occupied $G_{t, \text{occ}}$ and free $G_{t, \text{free}}$ GMMs are transformed to the world frame using the pose T_t . Then, these GMMs are inserted into the R-tree to create the local map G_t .

SPGF* (Lines 8 to 20 in Alg. 1): The SPGF* algorithm constructs an occupied GMM $G_{t, \text{occ}}$ and a compact free GMM basis $F_{t, \text{free}}$ by processing one scanline (*i.e.*, a row of pixels) at a time in a *single pass* through the entire depth image Z_t . Note that measurements that are neighbors in the 3D world are also neighbors in the 2D depth image. Thus, SPGF* exploits this property to efficiently infer surface geometries so that the accuracy and compactness of the GMM are maintained compared to prior *multi-pass* approaches [11]–[16].

SPGF* is an extension of our prior work SPGF [18] which is summarized as follows. As illustrated in Fig. 3, each scanline is denoted by L_v , where v is the row index. In Scanline Segmentation (SS, Line 12), pixels from each scanline are

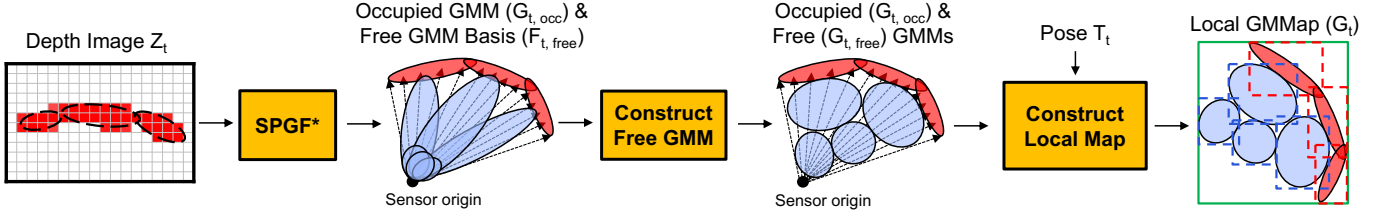


Fig. 2. **Per-image GMM construction:** Constructing a local GMMMap G_t that accurately represents both occupied and free regions from the current depth image Z_t obtained at pose T_t . Rays associated with each pixel in the depth image are illustrated with dotted arrows. Occupied and free GMMs are illustrated with red and blue ellipsoids, respectively. Dotted rectangles in the map G_t represent the bounding boxes at the leaf nodes of the R-tree. The green rectangle represents the bounding box at the root node of the R-tree that encloses the entire map G_t .

Algorithm 1: Per-Image GMM Construction

```

Input: Depth image  $Z_t$ , pose  $T_t$ 
Output: Local GMMMap  $G_t$ 
1 function constructLocalGMM( $Z_t, T_t$ )
2    $G_{t,occ}, F_{t,free} \leftarrow \text{SPGF}^*(Z_t)$ 
3    $G_{t,free} \leftarrow \text{constructFreeGMM}(F_{t,free})$ 
4    $G_t \leftarrow G_{t,free} \cup G_{t,occ}$ 
5    $G_t \leftarrow \text{transform}(G_t, T_t)$ 
6    $G_t \leftarrow \text{constructRtree}(G_t)$ 
7   return  $G_t$ 
8 subfunction SPGF*( $Z_t$ )
9    $Q \leftarrow \emptyset, Q_{prev} \leftarrow \emptyset$ 
10  for ( $v = 0; v < V; v = v + 1$ ) {
11     $L_v \leftarrow \text{extractScanline}(Z_t, v)$ 
12     $S \leftarrow \text{scanlineSegmentation}(L_v)$ 
13    if  $v = 0$  then
14       $Q_{prev} \leftarrow S$ 
15    else
16       $Q_{prev}, Q_{comp} \leftarrow \text{segmentFusion}(Q_{prev}, S)$ 
17       $Q \leftarrow Q \cup Q_{comp}$ 
18   $Q \leftarrow Q \cup Q_{prev}$ 
19   $G_{t,occ}, F_{t,free} \leftarrow Q$ 
20  return  $G_{t,occ}, F_{t,free}$ 

```

partitioned into a set of line segments S such that each segment represent a locally planar surface with distinct orientation. In Segment Fusion (SF, Line 16), segments are fused across successive scanlines to form a set of completed Gaussians Q_{comp} (appended to output in Line 17) and incomplete Gaussians Q_{prev} (for fusion with the next scanline).

The implementation of SS and SF in SPGF* is almost identical to those in SPGF except for the following differences. Recall that each pixel in the depth image is a sensor ray that originates from the robot. In SPGF, only occupied GMM $G_{t,occ}$ is constructed using endpoints of the sensor rays from all depth pixels in the image. In particular, Eqn. (15) and (18) are used to construct each occupied Gaussian (say a_i) in SS and SF, respectively. Since we would like to construct Gaussians associated with the free region as well, SPGF* constructs two free Gaussians ϕ_j (using the entire sensor ray) and β_j (using normalized sensor ray with depth $z = 1$) concurrently with each occupied Gaussian a_i . Those free Gaussians are constructed using Eqn. (16) in SS and Eqn. (18) in SF. Thus, for SPGF*, each element in the set S , Q , Q_{prev} and Q_{comp} of Alg. 1 includes the occupied Gaussian a_j with its associated

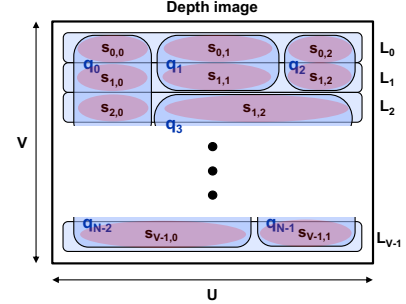
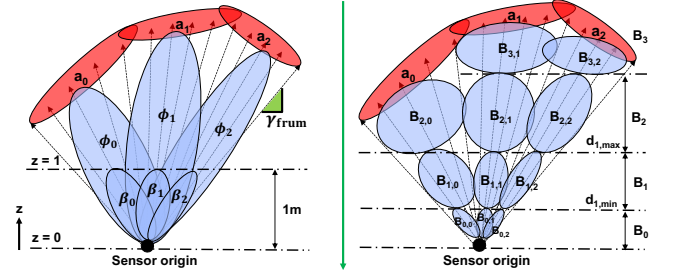


Fig. 3. Single-pass processing of the depth image in SPGF* for constructing the set of Gaussians Q where each element $q_j \in Q$ contains one occupied Gaussian a_j and a free Gaussian basis f_j . In Scanline Segmentation, each row (indexed by v) of the depth image is partitioned into a set of line segments $S = \{s_{v,i}\}$, which are fused across rows to form $q_j \in Q$ in Segment Fusion.



(a) Visualization of the free Gaussian basis $f_j = (\phi_j, \beta_j)$ associated with each occupied Gaussian a_j . These bases cannot represent the free region faithfully (e.g., near the obstacles). (b) Visualization of the free Gaussians $B_{i,j}$ that is recovered in subregion B_i from basis $f_j = (\phi_j, \beta_j)$. The set of all free Gaussians accurately represents the free region.

Fig. 4. Visualization of (a) the free Gaussian basis which can be used to recover (b) a corresponding set of free Gaussians in subregion B_i whose size increases with the distance from the sensor origin.

free Gaussians ϕ_j and β_j .

Fig. 4a illustrates the free Gaussians ϕ_j and β_j associated with each occupied Gaussian a_i . Note that the free Gaussians ϕ_j and β_j do not represent the free space traversed by the sensor rays very well. However, these free Gaussians can be used to reconstruct a better representation of free space as illustrated in Fig. 4b during the subsequent procedure. Thus, we define each free Gaussian basis f_j such that $f_j = (\phi_j, \beta_j)$. The set of all free Gaussian bases generated at the output of SPGF* forms the free GMM basis $F_{t,free}$.

Since the criteria for constructing and updating the Gaus-

sians in SPGF* is identical to SPGF, SPGF* inherits many desirable properties from SPGF. Since SS in Line 12 dominates SPGF* and can be executed independently for each scanline, SPGF* can be parallelized by concurrently executing SS for different scanlines across multiple CPU or GPU cores. Due to single-pass pixel-per-pixel processing in SS, only one pixel is stored in memory at any time. Thus, SPGF* is memory-efficient and avoids the storage of the entire depth image in memory as seen in most prior works.

Construct Free GMM (Alg. 2): In this section, we present Alg. 2 that directly generates the set of free Gaussians $G_{t,\text{free}}$ from their basis $F_{t,\text{free}}$. These Gaussians should accurately and compactly model the free space traversed by the sensor rays (*i.e.*, within the viewing frustum). In prior works [11], [12], the free Gaussians $G_{t,\text{free}}$ are inefficiently constructed from a large number of free-space points sampled at a fixed interval along all sensor rays. In contrast, the free Gaussians $G_{t,\text{free}}$ in GMM are directly constructed from their basis $F_{t,\text{free}}$ with little computational and memory overhead.

The free space is contained within the viewing frustum which is a pyramidal region with significantly different symmetries than each elliptical equipotential surface of the Gaussian distribution. Thus, as illustrated in Fig. 4a, free Gaussians (*i.e.*, ϕ and β) from the basis $F_{t,\text{free}}$ cannot faithfully represent the free region (especially near the obstacles). To achieve a more accurate representation, we partition the viewing frustum into subregions $\{B_0, B_1, \dots\}$ along the z -axis that is perpendicular to the image plane of the camera. Each subregion B_i is enclosed between two partitioning planes $z = d_{i,\text{max}}$ and $z = d_{i,\text{min}}$. As illustrated in Fig. 4b, free Gaussians are constructed to model each subregion separately.

The free Gaussians in each subregion (Fig. 4b) can be directly recovered from each basis $f = (\phi, \beta)$. Let the index i_f denote the *minimum index* across all subregions containing the endpoints of rays used to construct Gaussian ϕ . For instance, the index $i_f = 2$ for basis f_0 in Fig. 4. The subregion B_{i_f} is the difference between the region from sensor origin to the obstacle (represented by Gaussian ϕ) and the region from the sensor origin to the partitioning plane $d_{i_f,\text{min}}$ (represented by Gaussian β scaled to $d_{i_f,\text{min}}$). Each remaining subregion is the difference between regions from the sensor origin to two enclosing partitioning planes $d_{i_f,\text{min}}$ and $d_{i_f,\text{max}}$ (represented by Gaussian β scaled to $d_{i_f,\text{min}}$ and $d_{i_f,\text{max}}$). For each basis f , the parameters of the free Gaussian g (*i.e.*, first moment $m_g^{(1)}$, second moment $m_g^{(2)}$, normalizing constant ξ_g , and weight π_g) in subregion B_i are directly recovered from the *differences* between parameters of Gaussians ϕ and β as follows:

$$m_g^{(1)} = \begin{cases} m_\phi^{(1)} - d_{i,\text{min}}^2 m_\beta^{(1)}, & \text{if } i = i_f, \\ m_\beta^{(1)} (d_{i,\text{max}}^2 - d_{i,\text{min}}^2), & \text{if } 0 \leq i < i_f, \end{cases} \quad (19a)$$

$$m_g^{(2)} = \begin{cases} m_\phi^{(2)} - d_{i,\text{min}}^3 m_\beta^{(2)}, & \text{if } i = i_f, \\ m_\beta^{(2)} (d_{i,\text{max}}^3 - d_{i,\text{min}}^3), & \text{if } 0 \leq i < i_f, \end{cases} \quad (19b)$$

$$\xi_g = \pi_g = \begin{cases} \xi_\phi - d_{i,\text{min}} \xi_\beta, & \text{if } i = i_f, \\ \xi_\beta (d_{i,\text{max}} - d_{i,\text{min}}), & \text{if } 0 \leq i < i_f, \end{cases} \quad (19c)$$

See Fig. 4b for an illustration of the recovered free Gaussians $B_{i,j}$ in subregion B_i generated from basis f_j .

To retain high mapping fidelity, each subregion is sized according to its spatial resolution (*i.e.*, the density of the sensor rays) such that regions with higher resolution are modeled by smaller Gaussians. Since the sensor rays emanate outwards from the origin, the spatial resolution of each subregion B_i decreases as its index i increases (see Fig. 4b). To ensure that the maximum size of each Gaussian is inversely proportional to the spatial resolution, the distance between the partitioning planes that enclose each subregion B_i should increase with index i . Thus, given the maximum slope of the frustum's boundary γ_{frum} along the z axis (see Fig. 4a) and the initial distance d_0 between partitioning planes, the locations of these planes for each subregion B_i are computed as

$$d_{i,\text{max}} = d_0 \sum_{k=0}^{i-1} (\alpha_d \gamma_{\text{frum}})^k = \frac{d_0 ((\alpha_d \gamma_{\text{frum}})^i - 1)}{\alpha_d \gamma_{\text{frum}} - 1}, \quad (20a)$$

$$d_{i,\text{min}} = \begin{cases} 0, & \text{if } i = 0, \\ d_{i-1,\text{max}}, & \text{otherwise,} \end{cases} \quad (20b)$$

where α_d is a scaling parameter. We ensured $\alpha_d \gamma_{\text{frum}} > 1$ by choosing $\alpha_d = 0.5$ in all our experiments.

Although free Gaussians recovered from the basis can accurately model the free region, they are not as compact as the occupied GMM $G_{t,\text{occ}}$. Thus, after recovery, free Gaussians are fused with each other in each subregion to further enhance the compactness of the map. Alg. 2 efficiently performs Gaussian recovery and fusion. After sorting each basis f into its associated subregion based on index i_f (Line 4 to 8), free Gaussians are constructed within each subregion (from Line 9 onward) starting from the one that is furthestmost away from the sensor origin (see the green arrow in Fig. 4b). Using the bases, free Gaussians in each subregion B_i are initially recovered (Line 12 to 16) which are fused with each other using a region growing approach (Line 17 to 33).

During region growing, we need to ensure that the fused Gaussian can still accurately represent the free region within each subregion B_i . After fusing a free Gaussian q_g with its neighbor c_g (determined by whether their bounding boxes intersect in Line 19), we accept the fused Gaussian r_g (in Line 26) if it accurately represents its original components (*i.e.*, q_g and c_g). In prior works [11], the fused Gaussian r_g is accepted if the probabilistic distance d_h between two components q_g and c_g are below a pre-defined low threshold $\alpha_{h,\text{free}}$. Thus, only Gaussians that completely overlap the same region can be fused (see Fig. 5a). However, there exist many opportunities to fuse Gaussians that only partially overlap but accurately represent neighboring parts of the same region (see Fig. 5b). To also exploit these opportunities, our distance measure d_h is computed between the fused Gaussians r_g and its components $\{q_g, c_g\}$ using the Unscented Hellinger Distance [27] in Line 23. To maintain mapping accuracy, we scale the distance threshold $\alpha_{h,\text{free}}$ using the geometric similarity $s_r \in [0, 1]$ between Gaussians q_g and c_g in Line 25. The geometric similarity s_r between the two components is computed as the intersection over union ratio for the z dimension of their bounding boxes in Line 24.

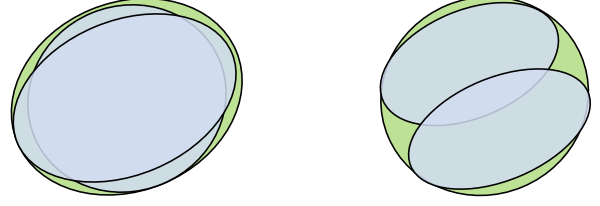
Algorithm 2: Free GMM Construction From Basis

```

Input: Free GMM basis  $F_{t,\text{free}}$ 
Output: Free GMM  $G_{t,\text{free}}$ 
1 function constructFreeGMM( $F_{t,\text{free}}$ )
2    $B \leftarrow \emptyset, G_{t,\text{free}} \leftarrow \emptyset$ 
3    $i_{\text{max}} \leftarrow 0$ 
4   // Sort basis using its subregion index  $i_f$ 
5   foreach  $f \in F_{t,\text{free}}$  do
6      $i_f \leftarrow \text{region}(f)$ 
7      $F_{t,\text{free}} \leftarrow F_{t,\text{free}} \setminus f$ 
8      $B_{i_f} \leftarrow B_{i_f} \cup f$ 
9      $i_{\text{max}} \leftarrow \max(i_{\text{max}}, i_f)$ 
10  for ( $i = i_{\text{max}}; i \geq 0; i = i - 1$ ) {
11    // See Eqn. (20)
12     $d_{i,\text{min}}, d_{i,\text{max}} \leftarrow \text{computePartitioningPlanes}(i)$ 
13     $Q \leftarrow \emptyset$ 
14    // Recover free Gaussians from bases
15    foreach  $f \in B_i$  do
16      // See Eqn. (19)
17       $g \leftarrow \text{recoverFreeGaussian}(f, d_{i,\text{min}}, d_{i,\text{max}})$ 
18       $B_i \leftarrow B_i \setminus f$ 
19       $q_g \leftarrow g, q_f \leftarrow f$ 
20       $Q \leftarrow Q \cup (q_g, q_f)$ 
21    // Fuse free Gaussians in subregion  $B_i$ 
22    while notEmpty( $Q$ ) do
23       $q \leftarrow \text{front}(Q)$ 
24       $C \leftarrow \text{findNeighbors}(Q, q)$ 
25      isFused  $\leftarrow$  false
26      foreach  $c \in C$  do
27        // See Eqn. (18)
28         $r \leftarrow \text{fuseGaussianAndBasis}(c, q)$ 
29         $d_h \leftarrow \text{unscentHellingerDistance}(r_g, c_g, q_g)$ 
30         $s_r \leftarrow \text{geometricSimilarity}(c_g, q_g)$ 
31        if  $d_h \leq s_r \cdot \alpha_{h,\text{free}}$  then
32           $q \leftarrow r$ 
33           $Q \leftarrow Q \setminus c$ 
34          isFused  $\leftarrow$  true
35      if isFused = false then
36         $Q \leftarrow Q \setminus q$ 
37         $G_{t,\text{free}} \leftarrow G_{t,\text{free}} \cup q_g$ 
38        // Propagate fusion decision to
39        // subregion  $B_{i-1}$ 
40        if  $i > 0$  then
41           $B_{i-1} \leftarrow B_{i-1} \cup q_f$ 
42  return  $G_{t,\text{free}}$ 

```

Even though free Gaussians are constructed to separately represent each subregion B_i , the fusion decision made between Gaussians (Line 25) in the current subregion B_i can be propagated to reduce the number of computations in subsequent subregions. The Gaussians recovered by the same basis across most subregions are almost relatively similar in shape (e.g., Gaussians $B_{2,1}$, $B_{1,1}$ and $B_{0,1}$ in Fig. 4b). Thus, the successful fusion between two Gaussians in the current subregion B_i (e.g., between $B_{2,1}$ and $B_{2,2}$) implies the same for other subregions B_{i-1}, \dots, B_0 (e.g., between $B_{1,1}$ and $B_{1,2}$, $B_{0,1}$ and $B_{0,2}$). To automatically propagate the fusion decision from the current subregion B_i , the fused basis q_f is simply transferred into the following subregions (B_{i-1}, \dots, B_0) at Line 33 across multiple iterations of the outer loop (Line 9).



(a) Fusion of two completely overlapping Gaussians (blue) into a single Gaussian (green).

(b) Fusion of two partially overlapping Gaussians (blue) into a single Gaussian (green).

Fig. 5. Our fusion criteria using the Unscented Hellinger Distance [27] allows for the creation of a single Gaussian (green) from two Gaussians (blue) when they (a) completely overlap to represent the same region or (b) partially overlap to represent neighboring parts of the same region in the environment.

Construct Local Map (Lines 4 to 6 in Alg. 1): To enable the fusion between the local GMMs (occupied $G_{t,\text{occ}}$ and free $G_{t,\text{free}}$) and the global map M_{t-1} in Section IV-C, local GMMs need to transform into the world frame as follows:

$$\mu_X \leftarrow R_t \mu_X + \epsilon_t, \quad \Sigma_X \leftarrow R_t \Sigma_X R_t^\top, \quad (21)$$

where R_t and ϵ_t are the rotation and translation matrix associated with pose T_t . The mean μ_X and covariance Σ_X for each Gaussian in the GMM are defined in Eqn. (3).

After the transformation, an R-tree is created for all Gaussians in Line 6 to form the local map G_t . First, a bounding box is constructed for each Gaussian to enclose its ellipsoidal bound as defined in Eqn. (12). Then, each Gaussian and its bounding box are inserted into the R-tree as shown in Fig. 2.

C. Globally-Consistent GMM Fusion

In this section, we present a novel memory-efficient procedure in Alg. 3 to directly update the global GMM M_{t-1} in place using Gaussians from the local GMM G_t . When the robot obtains a new depth image Z_t at timestep t , rays associated with a subset of pixels in the image traverse through a previously observed region C_t that is already modeled by the global map M_{t-1} . To ensure that the global map remains compact, these rays should be fused with the map to update the state of the region C_t .

In prior works [9], [10], [12], [17], the ray associated with each pixel in the image is casted into the global map to determine the location of the region C_t . Since each 640×480 depth image contains more than 300,000 rays, casting all rays requires a significant amount of time and accesses to off-chip DRAM where the map is stored. Since rays from the depth image are accurately compressed into a local GMM G_t , geometric properties of G_t are exploited to *i*) identify the location of the region C_t in the global map M_{t-1} with little memory access, and *ii*) directly update the region C_t using Gaussians in G_t to maintain the compactness and accuracy of the resulting global map M_t .

Fig. 6 illustrates the entire procedure for fusing the local map G_t into the global map M_{t-1} . Recall that from Section IV-B, Gaussians in the local map G_t are already transformed in the world frame and organized using an R-tree. Using the bounding box (at the root node of the R-tree)

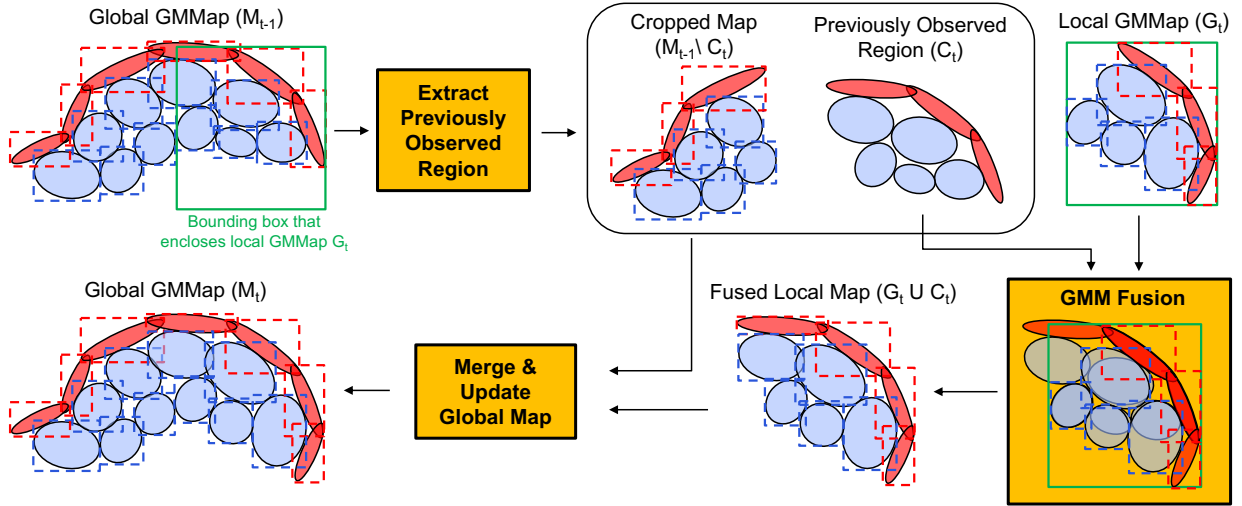


Fig. 6. **Globally-consistent GMM fusion:** Constructing the current global GMMMap M_t by fusing the local GMMMap G_t into the previous global GMMMap M_{t-1} . The bounding box (green rectangle) of local map G_t is used to determine the Gaussians C_t in the global map M_{t-1} that overlaps with G_t . Occupied and free GMMs are illustrated with red and blue ellipsoids, respectively. Dotted rectangles represent the bounding boxes at the leaf nodes of the R-tree.

Algorithm 3: Globally-Consistent GMM Fusion

```

Input: Local GMMMap  $G_t$ , previous global GMMMap  $M_{t-1}$ 
Output: Updated global GMMMap  $M_t$ 
1 function updateGlobalMap( $M_{t-1}, G_t$ )
2    $C_t \leftarrow \text{findObservedRegion}(G_t, M_{t-1})$ 
3    $M_{t-1} \leftarrow M_{t-1} \setminus C_t$ 
4    $M_{t-1} \leftarrow \text{updateRtree}(M_{t-1})$ 
5   foreach  $c \in C_t$  do
6     if isFreeGaussian( $c$ ) then
7        $Q \leftarrow \text{findIntersectingFreeGaussians}(G_t, c)$ 
8        $\alpha_h \leftarrow \alpha_{h, \text{free}}$ 
9     else
10       $Q \leftarrow \text{findIntersectingObsGaussians}(G_t, c)$ 
11       $\alpha_h \leftarrow \alpha_{h, \text{occ}}$ 
12     isObserved  $\leftarrow$  false
13     foreach  $q \in Q$  do
14        $r \leftarrow \text{fuseGaussians}(c, q)$  // See Eqn. (18)
15        $d_h \leftarrow \text{unscentedHellingerDistance}(r, c, q)$ 
16        $s_r \leftarrow \text{geometricSimilarity}(c, q)$ 
17       if  $d_h \leq s_r \cdot \alpha_h$  then
18          $c \leftarrow r$ 
19          $G_t \leftarrow G_t \setminus q$ 
20          $G_t \leftarrow \text{updateRtree}(G_t)$ 
21         isObserved  $\leftarrow$  true
22     if isObserved then
23        $C_t \leftarrow C_t \setminus c$ 
24        $G_t \leftarrow G_t \cup c$ 
25        $G_t \leftarrow \text{updateRtree}(G_t)$ 
26    $M_t \leftarrow M_{t-1} \cup C_t \cup G_t$ 
27    $M_t \leftarrow \text{updateRtree}(M_t)$ 
28   return  $M_t$ 

```

that encloses G_t , Gaussians in the previously observed region C_t can be extracted from the previous global map M_{t-1} in a *single traversal* through its R-tree (Line 2) without ray casting. After extraction, Gaussians in the region C_t are *directly* fused with the local map G_t (Lines 5 to 25). Since the Gaussians in C_t and G_t are extremely compact for storage within the

on-chip cache, the entire fusion process is expected to require little DRAM accesses. After completion, the fused local map (*i.e.*, $G_t \cup C_t$) is simply appended to the previous global map M_{t-1} in Line 26 to produce the updated global map M_t .

Our fusion process (Lines 5 to 25) enhances the compactness of the local map G_t while maintaining its accuracy. For each Gaussian $c \in C_t$, the R-tree in the local map G_t is used to efficiently search for the set of Gaussians Q that intersects with and represents the same type of region (*i.e.*, free or occupied) as c . In Line 14, the Gaussian c is fused with each neighbor $q \in Q$ into a fusion candidate r using Eqn. (18). Similar to Alg. 2, the fusion candidate r is accepted in Line 18 if the Unscented Hellinger Distance [27] between candidate r and its components $\{c, q\}$ is less than a distance threshold α_h . Recall that our fusion criteria can exploit a wide range of scenarios (*i.e.*, Fig. 5a and 5b) to enhance the compactness of the map. To maintain accuracy, we scale the distance threshold α_h in Line 17 using the geometric similarity s_r between components q and c . In Line 16, the similarity measure s_r between these components is computed as the intersection over union ratio of their 3D bounding boxes.

V. EXPERIMENTAL RESULTS & ANALYSIS

In this section, we compare our GMMMap against current state-of-the-art frameworks with different types of occupancy representations: OctoMap¹ [9] (discrete), NDT-OM² [10] (semi-parametric), and BGKOctoMap-L³ [17] (non-parametric). This comparison was performed using four diverse indoor and outdoor environments (*i.e.*, *Room*, *Warehouse*, *Soulcity*, and *Gascola*) generated from sequences of depth images and ground-truth poses.

Table I summarizes the characteristics of all four environments. In particular, *Room* (from real-world TUM-RGBD

¹<https://github.com/OctoMap/octomap>

²https://github.com/OrebroUniversity/perception_oru/tree/port-kinetic

³<https://github.com/RobustFieldAutonomyLab/la3dm>

datasets [28]) is a small structured environment that models crowded cubicles inside an office. *Warehouse* (from real-world TUM-RGBD datasets [28]) is a larger structured indoor environment captured using a longer and noisier range of the Kinect camera. In contrast, *Soulcity* (from synthetic TartanAir dataset [29]) is a large structured outdoor environment in a city containing several multi-story buildings with intricate sets of walkways. Finally, *Gascola* (from synthetic TartanAir dataset) is a large unstructured outdoor environment in a forest consisting of trees and a small hill.

To emulate an energy-constrained setting, all experiments were performed on the low-power NVIDIA Jetson TX2 platform in MAXP_CORE_ARM power mode [30]. All frameworks, implemented in C++, were compiled using the same settings. To reduce the memory overhead and map size, the floating point variables (and their associated operations) across all frameworks are stored as (and performed in) 32-bit single precision. Our single-core, multi-core, and GPU-accelerated GMMMap implementations (visualized in Open3D [31]) can be obtained at <https://github.com/mit-lean/GMMMap>.

Prior works achieve high mapping accuracy but are neither computationally nor memory efficient due to multi-pass processing of each depth image. In contrast, our GMMMap is highly accurate and memory efficient. Across a diverse set of indoor and outdoor environments, the mapping accuracy of GMMMap is comparable with prior works (Section V-A). In addition, our GMMMap is highly parallelizable and can be constructed in real-time at up to 81 images per second, which is $4\times$ to $146\times$ higher than prior works on the low-power Jetson TX2 platform (Section V-B). Due to single-pass depth image compression in SPGF* and directly operating on Gaussians during map construction, our GMMMap is extremely memory efficient. Compared with prior works (in Section V-C), our CPU implementation reduces *i*) the map size by at least 56%, *ii*) the memory overhead for storing input and temporary variables by at least 88%, and *iii*) the number of DRAM accesses by at least 78% during map construction. Thus, in Section V-D, the computational and memory efficiency of our GMMMap reduces energy consumption by at least 69% compared with prior works.

A. Accuracy of Occupancy Estimation

In this section, we compare the accuracy of the proposed GMMMap against NDT-OM, BGKOctoMap-L, and OctoMap. The hyperparameters of all frameworks are presented in Table II and are manually tuned to reduce the size of the maps

without significant deviation from their peak accuracy. For GMMMap, the hyperparameters are the unknown prior weight π_0 in Eqn. (4), the initial distance d_0 between partitioning planes in Eqn. (20), and the distance thresholds ($\alpha_{h,free}$ and $\alpha_{h,occ}$) for fusing Gaussians in Alg. 2 and 3. For NDT-OM, BGKOctoMap-L and OctoMap, the environment is voxelized so that the minimum voxel size is the hyperparameter. Since BGKOctoMap-L partitions the environment into equally-sized cubic blocks such that each block contains an octree (*i.e.*, defined as the test-data octrees [17]), the depth of the octree in each block is an additional hyperparameter. To generate compact training data representing the free region, BGKOctoMap-L samples points along each sensor ray at an interval dictated by the free resolution hyperparameter. A visual comparison for all the above-mentioned frameworks is presented in Fig. 7.

We use the receiver operating characteristics (ROC) curve to compare the accuracy across all frameworks. To generate the ROC curves, the occupancy probability is queried from each map at the locations of all measurements used to construct the map. In particular, measurements along each sensor ray are the ground-truth free regions, and the measurement at the end of each sensor ray is the ground-truth occupied region. By sweeping the thresholds for classifying occupied or free regions from each occupancy probability, the true positive rate (*i.e.*, the proportion of correct classifications during the prediction of occupied regions) of each map varies with the false positive rate (*i.e.*, the proportion of incorrect classifications during the prediction of the free regions). In addition, the area under the curve (AUC) represents the probability that the map estimates a higher occupancy for the occupied region than that of the free region. Thus, a map with high accuracy should generate a ROC curve that tends towards the upper-left corner of the plot to achieve a large AUC close to one.

Fig. 8 illustrates the ROC curve for each framework across all environments. The AUC associated with our GMMMap is slightly higher than other frameworks in structured indoor (*i.e.*, *Room* and *Warehouse*) and outdoor (*i.e.*, *Soulcity*) environments. These environments contain many locally planar surfaces that cannot be well-represented by cubic voxels in OctoMap and BGKOctoMap-L. Even though NDT-OM also utilizes Gaussians, they are constructed under the assumption that all measurements within each voxel belong to the same surface, and thus also suffer from voxelization artifacts when such assumption is invalid (*e.g.*, at corners of objects in Fig. 7i-b). Unlike other frameworks, our GMMMap does not require voxelization. During the SPGF* algorithm, the number of Gaussians and their associated parameters are accurately inferred from the continuity of planar surfaces from each depth image (*e.g.*, see Fig. 7i-a).

To achieve a compact representation and avoid modeling spurious measurements, SPGF* prunes away occupied Gaussians containing less than a certain number of measurements (*i.e.*, 200 in our experiments). In the unstructured *Gascola* environment, Gaussians representing many distant small surfaces (such as leaves) are mistakenly treated as spurious and thus pruned away (as illustrated in Fig. 7ii-a). However, in Fig. 8d, the accuracy of the GMMMap is still comparable with existing frameworks because the occupancy associated with

TABLE I
PROPERTIES OF ALL FOUR ENVIRONMENTS USED FOR EVALUATION.

Environment	Dimensions (m)	Images	Depth Image Resolution	Avg. Sensor Range (m)
Room (freiburg1_room)	11.28 × 12.05 × 3.45	1311	640×480	0.97
Warehouse (freiburg2_pioneer_slam)	23.52 × 17.90 × 4.29	2169	640×480	1.13
Soulcity	73.90 × 62.41 × 42.69	1083	640×480	10.85
Gascola	59.04 × 52.93 × 33.71	382	640×480	4.06

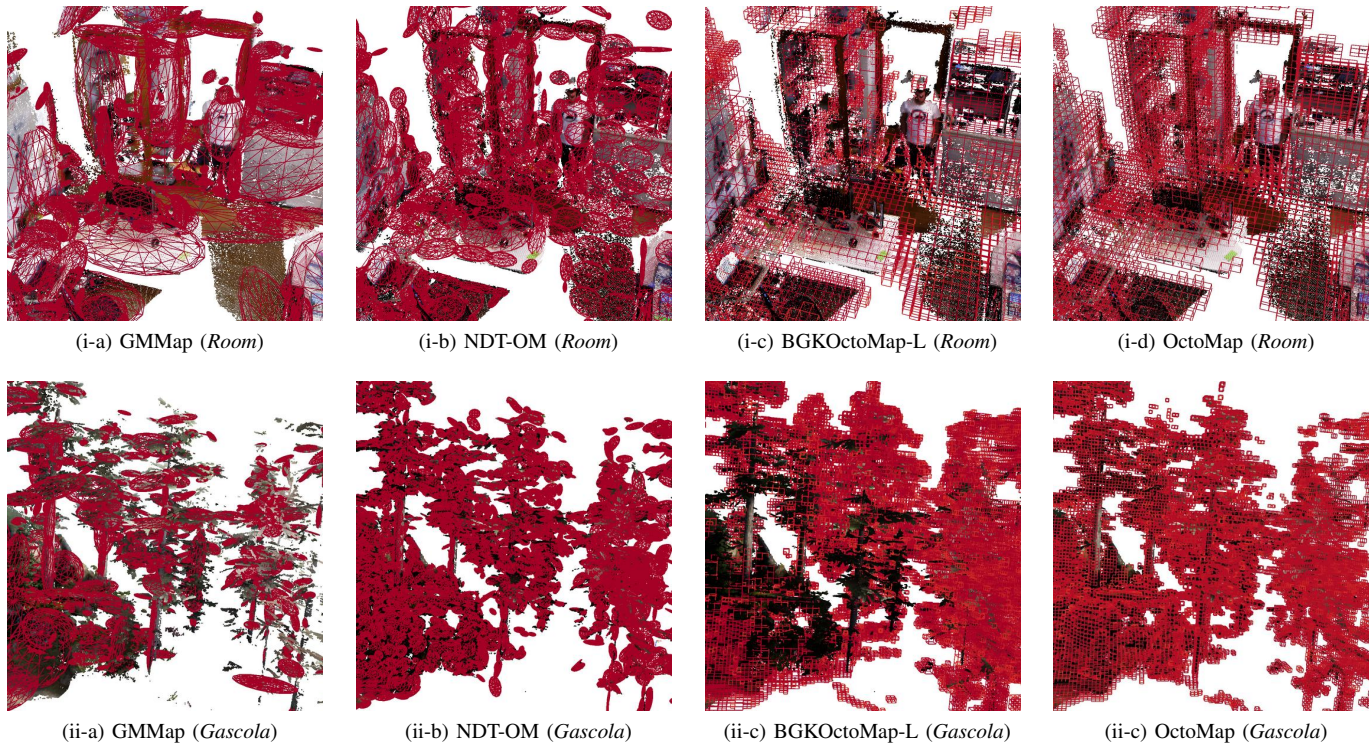


Fig. 7. Visualization of the (a) GMMMap, (b) NDT-OM, (c) BGKOctoMap-L, and (d) OctoMap overlaid over the ground-truth (i) *Room* (structured indoor) and (ii) *Gascola* (unstructured outdoor) environments. For GMMMap and NDT-OM, occupied Gaussians are visualized as wireframes of 3D ellipsoids. For BGKOctoMap-L and OctoMap, wireframes of voxels with an occupancy probability greater than 0.9 are visualized.

prune Gaussians can be partially recovered by regressing on other neighboring Gaussians. Unlike OctoMap which ignores the spatial correlation of the occupancy for all voxels, our GMMMap’s continuous representation can often exploit such correlation to infer occupancy in regions modeled by sparse measurements. Similar to other frameworks, our GMMMap can preserve the locations of unexplored regions. The visualization of GMMMap and the preservation of unexplored regions for *Warehouse* and *Soulcity* are illustrated in Fig. 9.

B. Construction & Query Throughput

In this section, we compare the computational efficiency of our GMMMap against other frameworks using the NVIDIA Jetson TX2 platform. The computational efficiency is evaluated in terms of the throughput for constructing the map (*i.e.*, depth images per second) and also querying the map (*i.e.*, locations per second). Table III summarizes these metrics for all frameworks across the four environments.

The NVIDIA Jetson TX2 platform contains a low-power ARM Cortex A57 CPU with four cores and a Pascal GPU with

two Streaming Multiprocessors (SMs). Due to computationally efficient GMM generation and fusion, our GMMMap can be constructed at a throughput of 11 to 18 images per second using only one CPU core, which is $4\times$ to $36\times$ higher than other frameworks. Since Scanline Segmentation (Line 12 in Alg. 1) dominates the amount of computation during map construction and can be concurrently executed across multiple rows of the depth image, our construction throughput can be significantly increased via parallelization. By using all four CPU cores, our multi-core implementation reaches a throughput of 31 to 60 images per second. Multi-core implementations of existing frameworks are either not publicly available or highly experimental. Even if these frameworks can be effectively parallelized with four cores, their throughputs are expected to be $4\times$ higher, which are still much lower than our multi-core implementation. By concurrently executing Scanline Segmentation across four images, our GPU implementation of GMMMap offers the highest construction throughput of 44 to 81 images per second, which is up to

TABLE II
PARAMETERS USED IN GMMAP, NDT-OM, BGKOCOTMAP-L, AND OCTOMAP ACROSS ALL FOUR ENVIRONMENTS.

Environment	Unknown Prior Weight (π_0)	Partition Plane Distance (d_0)	GMMMap		NDT-OM		BGKOctoMap-L		OctoMap
			Free Gaussian Fusion Threshold ($\alpha_{h,free}$)	Occupied Gaussian Fusion Threshold ($\alpha_{h,occ}$)	Voxel Size	Voxel Size	Free Resolution	Block Octree Depth	Voxel Size
Room	500,000	0.5m	0.26	0.70	0.4m	0.1m	0.3m	3	0.1m
Warehouse	500,000	0.5m	0.26	0.70	0.5m	0.1m	0.3m	3	0.2m
Soulcity	500,000	0.5m	0.63	1.41	1.2m	0.3m	3.0m	3	0.3m
Gascola	500,000	0.6m	0.63	1.41	1.2m	0.3m	3.0m	3	0.3m

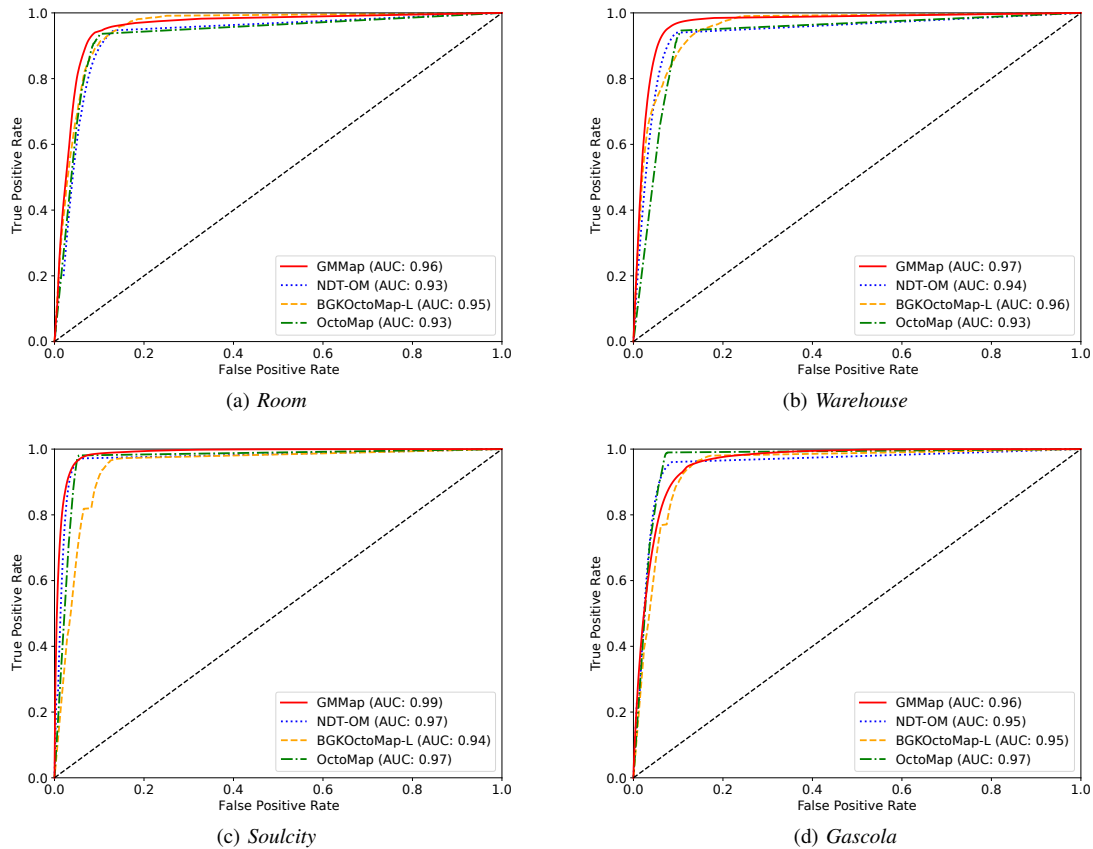


Fig. 8. Comparison of receiver operating characteristic (ROC) curves for the proposed GMMMap against OctoMap, NDT-OM, and BGKOctoMap-L in four environments: (a) *Room*, (b) *Warehouse*, (c) *Soulcity*, and (d) *Gascola*. The area under the ROC curve (AUC) equals to the probability that an occupied region is assigned a higher occupancy probability than the free region in the map.

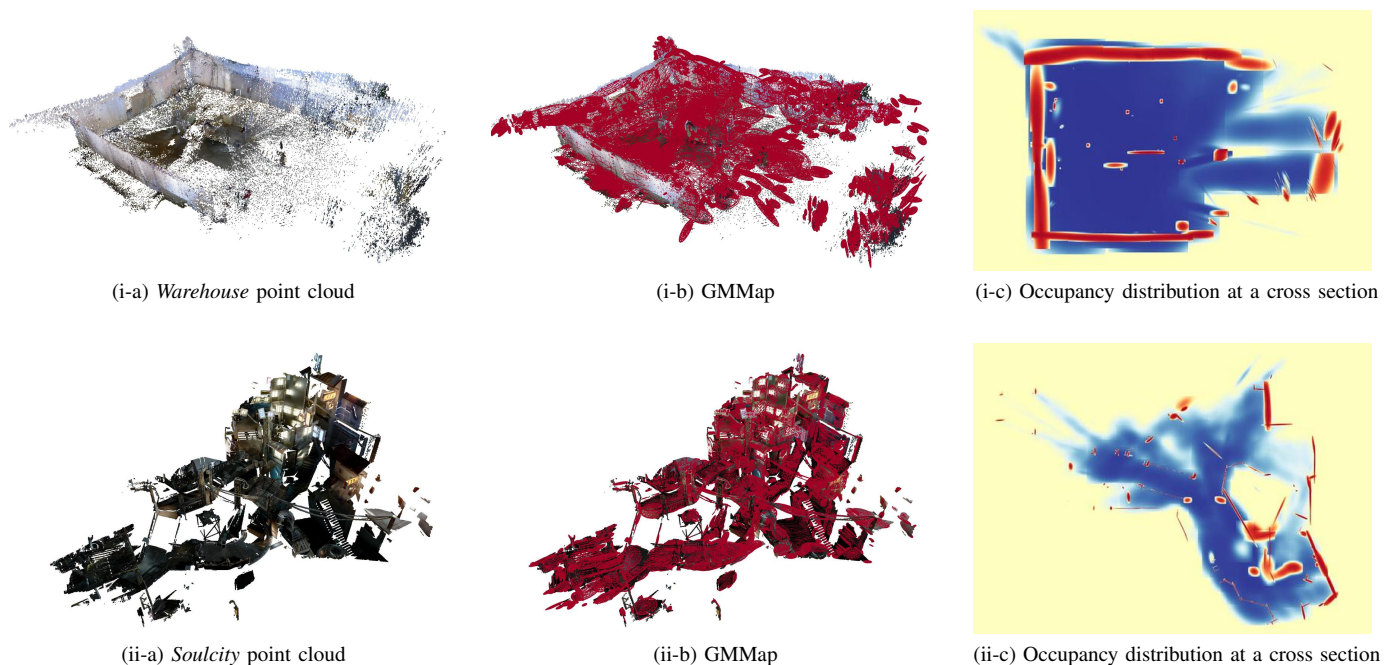


Fig. 9. Visualization of (a) the point cloud overlaid with its (b) GMMMap for (i) *Warehouse* (structured indoor) and (ii) *Soulcity* (structured outdoor) environments. For ease of visualization, only occupied Gaussians are shown for the GMMMap. In (c), the distribution of occupancy is visualized in the free regions (blue), unexplored regions (yellow), and occupied regions (red). The locations of the unexplored regions are well-preserved across both environments.

$2\times$ higher⁴ than our CPU multi-core implementation.

Finally, Table III also compares the query throughput of our GMMMap against existing frameworks. To emulate an energy-constrained setting during path planning, each map is queried at locations throughout all observed regions (*i.e.*, no unexplored regions) in the environment using only a single CPU core. Recall that each map consists of geometric primitives (*e.g.*, Gaussians or voxels) stored using a spatial data structure (*e.g.*, grid, R-tree, or octree). For existing frameworks, either traversing the spatial data structure (*i.e.*, accessing a voxel from a grid in NDT-OM) or inferring occupancy from primitives (*i.e.*, reading occupancy probability in BGKOctoMap-L and OctoMap) require little compute, which leads to high query throughputs ranging from 9.3×10^5 to 4.2×10^6 locations per second. However, in our GMMMap, both R-tree traversal and Gaussian Mixture Regression (GMR) require more computation. Thus, the query throughput is lower than other frameworks but still sufficiently high (ranging from 4.6×10^5 to 7.9×10^5 locations per second). If needed, the query throughput can be increased by accessing the map with multiple cores and/or partitioning the query locations into more localized sets for batch processing.

C. Memory Footprint

In this section, we compare the memory efficiency of our GMMMap against other frameworks when executing on the NVIDIA Jetson TX2 platform. In addition to the map size, we are interested in the memory overhead (for storing input and temporary variables) and the amount of DRAM access per

⁴Even though we are processing four images at the same time, the throughput is not four times higher because other sequential procedures of the GMMMap construction (*i.e.*, segment and GMM fusion) start to dominate.

pixel (which dictates DRAM energy consumption) during the map construction. Table III presents our results.

First, we compare the size of the map that includes the geometric primitives (*e.g.*, Gaussians and/or voxels) and the spatial data structure (*i.e.*, R-tree, grid and/or octree) among all frameworks. Due to the compactness and strong representational power of the Gaussians, NDT-OM achieves comparable accuracy while reducing the map size by 61% to 96% compared with BGKOctoMap-L and OctoMap. However, the extent of each Gaussian in NDT-OM is restricted by the constant voxel size across the entire environment. Thus, all Gaussians appear similarly sized as shown in Fig. 7. By using SPGF* to construct Gaussians that appropriately adapt to the geometries of occupied and free regions in the environment (see Fig. 7), our GMMMap achieves comparable accuracy while reducing the map size by 56% to 73% compared with NDT-OM. Across all frameworks, GMMMap requires the least amount of memory (167KB to 850KB) across all four environments.

In addition to map size, we are interested in the memory overhead (defined as the peak memory usage minus the map size) for storing input and temporary variables during map construction. For a memory-efficient framework, its memory overhead should be insignificant compared with the map size. Unfortunately, existing frameworks are not memory efficient. For NDT-OM, the memory overhead mostly comprises of the point cloud associated with each depth image (up to 3.6MB) for supporting a variety of edge cases during recency-weighted covariance update [10]. For BGKOctoMap-L, the memory overhead mostly is comprised of subsampled measurements in free and occupied regions (up to 21MB) for performing multi-pass BGK inference. For OctoMap, the memory overhead is mostly comprised of pointers to a large number of voxels intersected by sensor rays from each depth image (up to 1MB).

TABLE III

COMPARISON OF THE GMMAP AGAINST PRIOR WORKS USING THE NVIDIA JETSON TX2. ALL FRAMEWORKS ACHIEVE COMPARABLE ACCURACY.

Environment	Framework	Compute Resource (C = CPU core)	Throughput		Memory Footprint			Energy Consumption		
			Construction (images/s)	Query* (10^6 locations/s)	Map Size (KB)	Overhead (KB)	DRAM Access (bytes/pixel)	CPU & GPU (mJ/image)	DRAM (mJ/image)	Total (mJ/image)
Room	GMMMap	GPU & 4 C	81	0.79	167	24,563**	477	41	17	58
		4 C	60	0.79	176	41	27	36	16	52
	1 C	18	0.79	176	31	14	59	51	110	
	NDT-OM	1 C	5.0	3.5	426	3,146	160	202	157	359
	BGKOctoMap-L	1 C	2.8	0.93	4,935	7,101	242	352	272	624
	OctoMap	1 C	3.6	4.0	2,190	629	164	298	209	507
Warehouse	GMMMap	GPU & 4 C	73	0.52	268	24,596**	492	43	16	59
		4 C	58	0.51	269	56	30	37	14	51
	1 C	18	0.51	269	41	20	59	41	100	
	NDT-OM	1 C	3.7	3.7	614	3,436	199	273	209	482
	BGKOctoMap-L	1 C	0.5	1.4	13,811	21,265	940	1,888	1,463	3,351
	OctoMap	1 C	4.3	4.2	1,590	606	143	256	176	433
Soulcity	GMMMap	GPU & 4 C	60	0.46	850	24,740**	625	56	23	79
		4 C	31	0.47	838	128	76	73	25	98
	1 C	11	0.47	838	106	44	92	66	158	
	NDT-OM	1 C	3.1	3.9	1,925	4,391	372	324	248	572
	BGKOctoMap-L	1 C	0.8	1.0	23,265	5,502	596	1,204	926	2,130
	OctoMap	1 C	2.1	4.1	10,452	1,068	644	485	373	858
Gascola	GMMMap	GPU & 4 C	44	0.62	362	24,644**	1,048	69	36	105
		4 C	32	0.62	361	79	78	73	29	102
	1 C	11	0.62	361	63	54	97	81	178	
	NDT-OM	1 C	2.6	3.9	1,339	4,392	358	383	291	674
	BGKOctoMap-L	1 C	0.4	1.1	16,736	9,993	899	2,407	1,840	4,248
	OctoMap	1 C	1.6	3.9	9,376	760	1,136	634	494	1,129

* Unlike other metrics, query throughput is computed using a single CPU core. ** High memory overhead due to the necessary allocation of large GPU-accessible buffers (used to store input images and output results of Scanline Segmentation) for concurrent processing of four images. Allocations of these buffers are not required for CPU-only implementations.

In contrast, our GMMap requires very little memory overhead. Since SPGF* processes the depth image one pixel at a time in a single pass, only one (for single-core implementation) or four pixels (for multi-core implementation) are stored in memory at any time. Thus, the memory overhead associated with map construction is mostly comprised of compact line segments S from Scanline Segmentation in SPGF* and the local GMMap G_t generated at the output of Alg. 1. From Table III, the memory overhead of our single-core implementation is only 31KB to 106KB, which is at least 90% lower than other frameworks. Since four scanlines are segmented concurrently in our multi-core implementation, the memory overhead increases and ranges from 41KB to 128KB, which is at least 88% lower than other frameworks. However, our GPU implementation requires much larger memory overhead (around 24MB) due to the allocations of large GPU-accessible buffers for transferring four depth images and their Scanline Segmentation outputs to and from the GPU.

Finally, we compare the average amount of DRAM access required for integrating each measurement (*i.e.*, pixel in the depth image) into the map among all frameworks. The amount of DRAM access correlates with the energy consumption of the DRAM and is computed by multiplying the number of last-level cache misses (obtained from hardware counters) with the size of the cache line. Recall that existing frameworks update the map by incrementally casting each measurement ray (more than 300,000 rays in a 640×480 depth image) into the current map. Since these rays diverge away from the sensor origin, memory accesses along these rays often lack spatial and temporal locality (especially if the map is too large to fit within on-chip caches). Thus, the single-core implementations of existing frameworks require significant number of DRAM accesses ranging from 160 bytes to more than 1KB per pixel.

In contrast, our GMMap avoids ray casting by directly fusing Gaussians from a compact local map G_t with Gaussians in a compact global map M_{t-1} (see Fig. 6). Since a majority of the local and global map is expected to remain in cache, our single-core implementation reduces DRAM access by at least 85% (compared to existing frameworks) by accessing only 14 bytes to 54 bytes per pixel. Since multiple cores share the last-level cache, the number of cache misses increases for our multi-core implementation which requires slightly higher DRAM accesses ranging from 27 bytes to 78 bytes per pixel (at least 78% lower than existing frameworks). Our GPU implementation requires much larger DRAM accesses due to the higher amount of cache misses from the concurrent segmentation of all scanlines in four images. However, most DRAM accesses from our GPU implementation are coalesced (*i.e.*, multiple accesses can be serviced with a single transaction). Thus, the energy consumption of the DRAM slightly increases compared with our multi-core CPU implementation.

D. Energy Consumption

Table III summarizes the average energy consumption per depth image during map construction. Across all frameworks, the energy consumption of the DRAM is significant compared with that of CPU and GPU, which underscores the

importance of reducing memory overhead and access. Due to computationally efficient single-pass GMM creation and fusion, the energy consumption of the CPU in our single-core implementation is reduced by at least 71% compared with other frameworks. By avoiding ray casting (and its associated DRAM accesses), the energy consumption of the DRAM in our single-core implementation is reduced by at least 68% compared with existing frameworks. Our multi-core and GPU implementations are even more energy efficient because the static power consumption of the CPU, GPU, and DRAM are amortized across multiple cores and/or SMs. Thus, the total energy consumption of our CPU single-core, CPU multi-core, and GPU implementations are reduced by at least 69%, 83%, and 84% compared with existing frameworks, respectively.

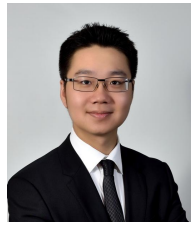
VI. CONCLUSION

In this work, we proposed the GMMap that uses a compact Gaussian Mixture Model to accurately model the continuous distribution of occupancy in 3D environments. Occupancy probability is inferred with Gaussian Mixture Regression which is extended to retain unexplored regions. In contrast with prior works, novel algorithms are proposed to achieve real-time map construction on energy-constrained platforms while significantly reducing memory overhead and access. When benchmarked on the low-power NVIDIA Jetson TX2 platform across a diverse set of environments, GMMap can be constructed at a throughput of up to 60 images per second using the CPU and up to 81 images per second using the GPU, which is $4\times$ to $146\times$ higher than prior works. While achieving comparable accuracy as prior works, our CPU implementation of GMMap reduces map size by at least 56%, memory overhead by at least 88%, DRAM access by at least 78%, and energy consumption by at least 69%. Thus, to the best of our knowledge, GMMap not only enables real-time large-scale 3D mapping for energy-constrained robots for the first time but also illustrates the significance of memory-efficient algorithms for enabling low-power autonomy on these robots.

REFERENCES

- [1] K. P. Valavanis and G. J. Vachtsevanos, *Handbook of unmanned aerial vehicles*. Springer, 2015, vol. 2077.
- [2] M. Keennon, K. Klingebiel, and H. Won, "Development of the nano hummingbird: A tailless flapping wing micro air vehicle," in *50th AIAA aerospace sciences meeting including the new horizons forum and aerospace exposition*, 2012, p. 588.
- [3] R. He, S. Sato, and M. Dreha, "Design of single-motor nano aerial vehicle with a gearless torque-canceling mechanism," in *46th AIAA Aerospace Sciences Meeting and Exhibit*, 2008, p. 1417.
- [4] M. Horowitz, "1.1 computing's energy problem (and what we can do about it)," in *2014 IEEE International Solid-State Circuits Conference Digest of Technical Papers (ISSCC)*, 2014, pp. 10–14.
- [5] B. Yamauchi, "A frontier-based approach for autonomous exploration," in *IEEE International Symposium on Computational Intelligence in Robotics and Automation*, 1997, pp. 146–151.
- [6] Z. Zhang, T. Henderson, S. Karaman, and V. Sze, "Fsmi: Fast computation of shannon mutual information for information-theoretic mapping," *The International Journal of Robotics Research*, vol. 39, no. 9, pp. 1155–1177, 2020.
- [7] T. Henderson, V. Sze, and S. Karaman, "An efficient and continuous approach to information-theoretic exploration," in *2020 IEEE International Conference on Robotics and Automation (ICRA)*. IEEE, 2020, pp. 8566–8572.

- [8] S. Karaman and E. Frazzoli, "Sampling-based algorithms for optimal motion planning," *The international journal of robotics research*, vol. 30, no. 7, pp. 846–894, 2011.
- [9] A. Hornung, K. M. Wurm, M. Bennewitz, C. Stachniss, and W. Burgard, "Octomap: An efficient probabilistic 3d mapping framework based on octrees," *Autonomous robots*, vol. 34, no. 3, pp. 189–206, 2013.
- [10] J. P. Saariinen, H. Andreasson, T. Stoyanov, and A. J. Lilienthal, "3d normal distributions transform occupancy maps: An efficient representation for mapping in dynamic environments," *The International Journal of Robotics Research*, vol. 32, no. 14, pp. 1627–1644, 2013.
- [11] V. Guizilini and F. Ramos, "Towards real-time 3d continuous occupancy mapping using hilbert maps," *The International Journal of Robotics Research*, vol. 37, no. 6, pp. 566–584, 2018.
- [12] S. Srivastava and N. Michael, "Efficient, multifidelity perceptual representations via hierarchical gaussian mixture models," *IEEE Transactions on Robotics*, vol. 35, no. 1, pp. 248–260, 2018.
- [13] B. Eckart, K. Kim, A. Troccoli, A. Kelly, and J. Kautz, "Accelerated generative models for 3d point cloud data," in *Proceedings of the IEEE conference on computer vision and pattern recognition*, 2016, pp. 5497–5505.
- [14] C. O'Meadhra, W. Tabib, and N. Michael, "Variable resolution occupancy mapping using gaussian mixture models," *IEEE Robotics and Automation Letters*, vol. 4, no. 2, pp. 2015–2022, 2018.
- [15] A. Dhawale and N. Michael, "Efficient parametric multi-fidelity surface mapping," in *Robotics: Science and Systems (RSS)*, vol. 2, no. 3, 2020, p. 5.
- [16] K. Goel, N. Michael, and W. Tabib, "Probabilistic point cloud modeling via self-organizing gaussian mixture models," *IEEE Robotics and Automation Letters*, vol. 8, no. 5, pp. 2526–2533, 2023.
- [17] K. Doherty, T. Shan, J. Wang, and B. Englot, "Learning-aided 3-d occupancy mapping with bayesian generalized kernel inference," *IEEE Transactions on Robotics*, pp. 1–14, 2019. [Online]. Available: <https://doi.org/10.1109/tro.2019.2912487>
- [18] P. Z. X. Li, S. Karaman, and V. Sze, "Memory-efficient gaussian fitting for depth images in real time," in *2022 International Conference on Robotics and Automation (ICRA)*. IEEE, 2022, pp. 8003–8009.
- [19] A. Elfes, "Sonar-based real-world mapping and navigation," *IEEE Journal on Robotics and Automation*, vol. 3, no. 3, pp. 249–265, 1987.
- [20] B.-J. Ho, P. Sodhi, P. Teixeira, M. Hsiao, T. Kusnur, and M. Kaess, "Virtual occupancy grid map for submap-based pose graph slam and planning in 3d environments," in *2018 IEEE/RSJ International Conference on Intelligent Robots and Systems (IROS)*. IEEE, 2018, pp. 2175–2182.
- [21] S. T. O'Callaghan and F. T. Ramos, "Gaussian process occupancy maps," *The International Journal of Robotics Research*, vol. 31, no. 1, pp. 42–62, 2012.
- [22] J. Wang and B. Englot, "Fast, accurate gaussian process occupancy maps via test-data octrees and nested bayesian fusion," in *2016 IEEE International Conference on Robotics and Automation (ICRA)*, May 2016, pp. 1003–1010.
- [23] F. Ramos and L. Ott, "Hilbert maps: Scalable continuous occupancy mapping with stochastic gradient descent," *The International Journal of Robotics Research*, vol. 35, no. 14, pp. 1717–1730, 2016.
- [24] H. G. Sung, *Gaussian mixture regression and classification*. Rice University, 2004.
- [25] A. Guttman, "R-trees: A dynamic index structure for spatial searching," in *Proceedings of the 1984 ACM SIGMOD international conference on Management of data*, 1984, pp. 47–57.
- [26] D. W. Scott and W. F. Szewczyk, "From kernels to mixtures," *Technometrics*, vol. 43, no. 3, pp. 323–335, 2001.
- [27] M. Kristan and A. Leonardis, "Multivariate online kernel density estimation," in *Computer Vision Winter Workshop*, 2010, pp. 77–86.
- [28] J. Sturm, N. Engelhard, F. Endres, W. Burgard, and D. Cremers, "A benchmark for the evaluation of rgb-d slam systems," in *Proc. of the International Conference on Intelligent Robot Systems (IROS)*, Oct. 2012.
- [29] W. Wang, D. Zhu, X. Wang, Y. Hu, Y. Qiu, C. Wang, Y. Hu, A. Kapoor, and S. Scherer, "Tartanair: A dataset to push the limits of visual slam," in *2020 IEEE/RSJ International Conference on Intelligent Robots and Systems (IROS)*. IEEE, 2020, pp. 4909–4916.
- [30] "Jetson Download Center," NVIDIA Developer, available: <https://developer.nvidia.com/jetson-tx2-nx-system-module-data-sheet>.
- [31] Q.-Y. Zhou, J. Park, and V. Koltun, "Open3D: A modern library for 3D data processing," *arXiv:1801.09847*, 2018.



Peter Zhi Xuan Li (Student Member, IEEE) received the B.A.Sc. in Engineering Science from the University of Toronto, Canada, in 2018. Between 2016 and 2017, he worked in the High-Speed Converters Group at Analog Devices, Toronto, as an integrated circuit engineer. His research focuses on the co-design of algorithms and specialized hardware for localization, mapping, and path-planning on energy-constrained miniature robots.



Sertac Karaman (Member, IEEE) received the B.S. degrees in mechanical engineering and computer engineering from the Istanbul Technical University, Istanbul, Turkey, in 2007, the S.M. degree in mechanical engineering and the Ph.D. degree in electrical engineering and computer science from the Massachusetts Institute of Technology (MIT), Cambridge, MA, USA, in 2009 and 2012, respectively. He is currently an Associate Professor of Aeronautics and Astronautics with MIT. His research interests include the broad areas of robotics and control

theory. In particular, he is focusing on the applications of probability theory, stochastic processes, stochastic geometry, formal methods, and optimization for the design and analysis of high-performance cyber-physical systems. The application areas of his research include driverless cars, unmanned aerial vehicles, distributed aerial surveillance systems, air traffic control, certification and verification of control systems software, and many others.

Dr. Karaman was the recipient of the IEEE Robotics and Automation Society Early Career Award, in 2017, the Office of Naval Research Young Investigator Award, in 2017, the Army Research Office Young Investigator Award, in 2015, the National Science Foundation Faculty Career Development (CAREER) Award, in 2014, the AIAA Wright Brothers Graduate Award, in 2012, and the NVIDIA Fellowship, in 2011.



Vivienne Sze (Senior Member, IEEE) received the B.A.Sc. (Hons) degree in electrical engineering from the University of Toronto, Toronto, ON, Canada, in 2004, and the S.M. and Ph.D. degree in electrical engineering from the Massachusetts Institute of Technology (MIT), Cambridge, MA, in 2006 and 2010 respectively. In 2011, she received the Jin-Au Kong Outstanding Doctoral Thesis Prize in Electrical Engineering at MIT.

She is an Associate Professor at MIT in the Electrical Engineering and Computer Science Department. Her research interests include computing systems that enable energy-efficient machine learning, computer vision, and video compression/processing for various applications, including autonomous navigation, digital health, and the Internet of Things. Prior to joining MIT, she was a Member of the Technical Staff in the Systems and Applications R&D Center at Texas Instruments (TI), Dallas, TX, where she designed low-power algorithms and architectures for video coding. She also represented TI in the Joint Collaborative Team on Video Coding (JCT-VC).

Dr. Sze was a recipient of the Air Force Young Investigator Research Program Award, the DARPA Young Faculty Award, the Edgerton Faculty Award, several faculty awards from Google, Facebook, and Qualcomm, the 2021 University of Toronto Engineering Mid-Career Achievement Award, and the 2020 ACM-W Rising Star Award, and a co-recipient of the 2018 Symposium on VLSI Circuits Best Student Paper Award, the 2017 CICC Outstanding Invited Paper Award, and the 2016 IEEE Micro Top Picks Award. She was a member of the JCT-VC team that received the Primetime Engineering Emmy Award for the development of the HEVC video compression standard.

VII. BIOGRAPHY